

Novel Prototype of a Compton Camera Based on a Monolithic GAGG Crystal*

Lin Song,¹ Hao-Tian Qi,¹ and Li-Hua Zhu^{1,†}

¹*Beihang University, Beijing 100191, China*

Traditional scintillator-based or semiconductor-based Compton Cameras generally use the method of pixelation detector to obtain the interaction position of γ -rays with detectors, which suffers from the disadvantages of complex process, high cost, strong dependence on pixelation size for position resolution, and huge electronic readout system. These disadvantages limit the development of miniaturization and commercialization of Compton Cameras. In this study, we used the whole GAGG crystal coupled Silicon Photomultiplier (SiPM) array to build two types of detectors, which are Side-readout type detector and Back-readout type detector, and developed two kinds of position reconstruction algorithm, the Response Function Method and the Photon Distribution Reconstruction Method. The position resolution of the two types of detectors was evaluated, and the position resolution of the Side-readout type detector and Back-readout type detector was 1.2 mm and 1.6 mm, respectively. In addition, we built a prototype of a double-layer Compton Camera based on a monolithic GAGG crystal using a Side-readout type detector as a scattering detector and a Back-readout type detector as an absorption detector. The position resolution of locating the radioactive source is 5.4 mm with the source placing 27 mm away from the scattering detector.

Keywords: Compton Camera, Scintillator, Position Reconstruction, SiPM

I. INTRODUCTION

Compton Cameras use the principle of Compton scattering to locate where γ -rays are generated. It has unique advantage in detection efficiency compared with other gamma-ray imaging modalities since no mechanical collimation structure is needed.[1] Compton Cameras are widely used in the fields of biomedical and radiation environmental monitoring.[2–7]

In response to the enormous market demand, several foreign companies have carried out research and development of Compton Camera, and have successively released related products, such as United States H3D company released H100[8], PHDS company released GEGI[9], Japan Institute of Aerospace Sciences (ISAS) released ASTROCAM[10], etc. Among them, ASTROCAM has been tested on-site in Fukushima and has proven its capability for hot spot detection and radioactive decontamination assessment. The domestic Compton Camera imaging technology research is still in the development stage, and related simulation and image reconstruction algorithm research has been carried out one after another, such as: Guo Xiaofeng et al.[11] have carried out research on the Compton Camera composed of CZT detector based on Geant4. Some laboratories have built Compton Camera prototypes, such as Liu Yilin[12], Tsinghua University, built Compton Cameras based on 4×4 pixel 3-D CZT detectors; Zhang Jipeng et al.[13], Institute of High Energy Chinese Academy of Sciences, constructed a double-layer Compton Camera based on GAGG crystal and SiPM array. However, self-developed Compton Camera products that can be put on the market are still blank.

At present, whether it is scintillator-based or semiconductor-based Compton cameras, the interaction

position of γ -rays is obtained by pixelating the detector[14–18]. Although the principle of this method is simple, it has obvious limitations that the reconstruction accuracy is completely dependent on the degree of pixelation of the detector. Scintillator crystals are prone to cracking and shattering during processing, making it difficult to obtain crystal arrays with small pixel sizes. Although semiconductor detectors can obtain small pixel sizes, semiconductor detectors themselves are expensive and difficult to promote. At the same time, both scintillator detection and semiconductor detection face a serious problem after increasing the degree of pixelation, that is, the unusually large electronic readout system. A bold and novel idea is to use a monolithic scintillator crystal for position reconstruction, which has the characteristics of simple structure, low cost, and easy storage compared with pixelated scintillator crystal arrays. There are very few reports of the use of monolithic scintillator crystals in Compton Cameras, mainly because it is difficult to confirm where γ -rays interact in the monolithic crystal. In recent years, with the increasing application of SiPM, this problem seems to be solvable. Traditional Compton Cameras use photomultiplier tubes (PMTs) as photoconversion devices, but PMTs are expensive, bulky and require high voltage, which cannot meet the needs of commercial Compton Cameras for low cost and miniaturization[19]. In contrast, SiPMs are small in size, high in gain, low in operating voltage, insensitive to magnetic fields, high in photon detection efficiency, and most importantly, they can be combined into any shape of detection arrays for use[20–23].

In this study, we constructed two types of detectors using the monolithic crystal coupled SiPM arrays to reconstruct the interaction position of γ -rays in the monolithic scintillator. The VMEDAQ system was used to obtain the relevant information of the interaction events in the detector. Two kinds of position reconstruction algorithm were developed to reconstruct the interaction positions of the events in the crystal, and the position resolution performance of the two types of detectors was evaluated experimentally. We used two types of

* Supported by the National Natural Science Foundation of China (No.U1867210)

† Corresponding author, Li-Hua Zhu, Beihang University, 13520056359, zhulh@buaa.edu.cn.

70 detectors as scattering detectors and absorption detectors for
 71 Compton Cameras, respectively, and developed a new proto-
 72 type of Compton Camera, and experimentally tested the per-
 73 formance of this prototype.

74

II. EQUIPMENTS

75

A. The experimental equipment

76 Scintillators, such as NaI, CsI, Cerium-doped Gadolinium
 77 Aluminum Gallium Garnet(GAGG), LYSO, and LaBr₃, are
 78 often used in Compton cameras due to their relatively high de-
 79 tector efficiency and the fast time response.[24] The crystals
 80 used in this study were GAGG. Compared with other crys-
 81 tals, GAGG has the following advantages: 1. unlike NaI and
 82 LaBr₃, GAGG shows no non-hygroscopicity in air and does
 83 not need to be packaged; 2. Different from LYSO and LaBr₃,
 84 GAGG produces no internal background radiation; 3. GAGG
 85 has a higher luminescence yield and a shorter luminescence
 86 duration than the cases in CsI, which is conducive to improve
 87 the signal-to-noise ratio and energy resolution.[25, 26]

88 Traditional Compton Cameras use a pixelated crystal con-
 89 figuration, and the detector must be attached to the back of the
 90 crystal to match each pixel to get position information.[27]
 91 However, as a scattering detector, the Back-readout type de-
 92 tector will inevitably affect the outgoing γ -rays after interact-
 93 ing with the scattering detector, resulting in poor reconstruc-
 94 tion results.In this study, a monolithic crystal was used, so a
 95 novel configuration the side-readout detector (referred to as
 96 S-type, figure 1.b) could be employed.At the same time, a
 97 Back-readout type detector (referred to as B-type, figure 1.c)
 98 was also built and used as an absorption detector for Compton
 99 Cameras. The S-type detector uses a 27*27*3 mm³ GAGG
 100 crystal coupled with four 1*8 SiPM arrays(figure 1.a), and
 101 each SiPM is read out separately, with a total of 32 signals.
 102 The B-type detector uses a 27*27*2 mm³ GAGG crystal cou-
 103 pled with an 8*8 SiPM array. The 8-channel SiPMs in hor-
 104 izontal of the 8*8 array are added into one signal output, so
 105 we get 8 outputs in horizontal. Similarly,the 8-channel SiPMs
 106 in longitudinal are added into one signal output, so we get 8
 107 outputs in longitudinal. SensL's C-60035 pixel SiPM was se-
 108 lected, which has a pixel area of 3*3 mm². There are 10,998
 109 micropixel APDs within each pixel, and each micropixel is 20
 110 μm *20 μm in size. A double-layer Compton camera based on
 111 monolithic crystals was built, with an S-type detector as the
 112 scattering detector and a B-type detector as the absorption de-
 113 tector(figure 1.e). The distance between the scattering detec-
 114 tor and the absorption detector is adjustable, and the distance
 115 used in this experiment is 20 mm. VMEDAQ is used to filter
 116 the coincidence events and log the amplitude of the signal.

117

B. The S-type and B-type detector

118 The Cs-137 spectra measured by the S-type detector with
 119 and without the reflective layer are shown in figure 2(a,b), and
 120 the reflective layer material is polytetrafluoroethylene. More

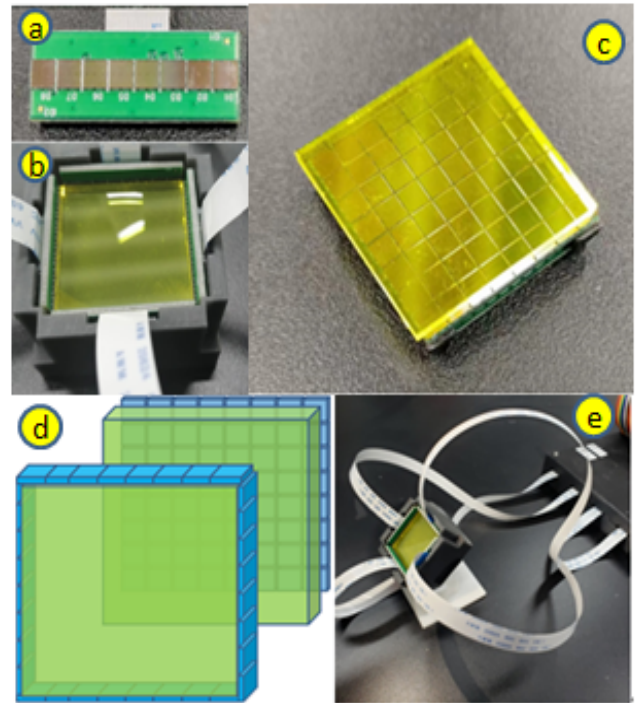


Fig. 1. a.1*8 SiPM array; b. S-type detector; c. B-type detector; d. the schematic diagram of the Compton camera; e. the prototype of the Compton camera

121 fluorescent photons are collected when the reflective layer is
 122 wrapped, so the total energy peak address when the reflec-
 123 tive layer is wrapped is significantly higher than that when
 124 the reflective layer is not wrapped. The resolution of the to-
 125 tal energy peak is 8.2% when the reflective layer is wrapped,
 126 which is very close to the performance index value given by
 127 the crystal manufacturer. The energy resolution drops to 9.4%
 128 when don't wrap the reflective layer. The reflection layer has
 129 very little effect on the energy resolution of S-type detectors

130 Due to the fact that the reflective layer is not completely
 131 smooth, the fluorescent photons are diffusely reflected by the
 132 reflector layer during transmission, so the interaction position
 133 information carried by them is destroyed. To study the im-
 134 pact of this destruction on S-type detector, we recorded the
 135 outputs of 32-channel SiPMs by irradiating the middle of the
 136 GAGG crystal vertically from a α source in two cases :with
 137 and without the reflective layer. As mentioned above, without
 138 reflective layer results in a slight reduction of the total energy
 139 peak address, so the amplification of the amplifier is slightly
 140 increased without the reflective layer. A similar operation is
 141 performed at B-type detector. For the S-type detector, 32-
 142 channel SiPMs are distributed on the four sides of the crystal.
 143 Due to the central symmetry, Figure 3(a,b) shows the spec-
 144 trum of only 8-channel SiPMs on one side. The spectrum of
 145 SiPMs in the same geometric position on the left and right are
 146 very similar due to the left-right symmetry, so the spectrum of
 147 the 8-channel SiPMs can be divided into 4 groups. It can be
 148 seen that the spectrum difference between the four groups of
 149 SiPMs is not obvious when there is a reflective layer, which

150 will bring great uncertainty to reconstruct the interaction position. In the other hand if we don't wrap the reflective layer, 151 the spectrum of the four groups of SiPMs has obvious differences, which is very beneficial for the determination of the 152 interaction position.

153 For the S-type detector, the reflection layer only slightly 154 improves energy resolution, but greatly reduces position resolution. In order to obtain better position resolution, the de- 155 sign of the S-type detector without the reflective layer was 156 adopted.

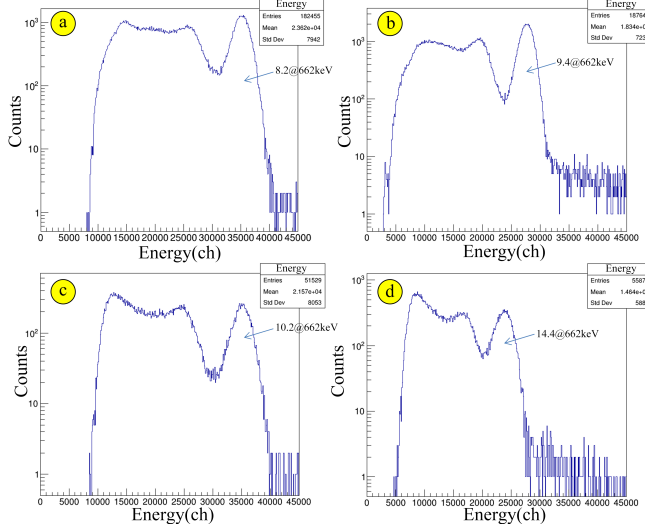


Fig. 2. The Cs-137 spectra of the S-type detector: with the reflective layer(a), without the reflective layer(b);The Cs-137 spectra of the B-type detector: with the reflective layer(c), without the reflective layer(d)

160 The Cs-137 spectra measured by the B-type detector with 161 and without the reflective layer are shown in figure 2(c,d), and 162 the reflective layer material is polytetrafluoroethylene. Same as 163 the S-type detector, for the B-type detector more fluorescent 164 photons are collected, so the total energy peak address when 165 the reflective layer is wrapped is higher,too. The energy res- 166 olution of the B-type detector is worse than that of the S-type 167 detector no matter with or without the reflective layer. The 168 main reason is that the B-type detector uses more SiPMs, and 169 the impact of SiPM response inconsistent is greater. At the 170 same time, the readout of the B-type detector in this study 171 isn't one by one, but additive readout. The difference be- 172 tween additive circuits can also lead to a decrease in energy 173 resolution.

174 The reflective layer reduces the energy resolution from 175 10.2% to 14.4% , which is a obvious reduction. It seems 176 that the design of the B-type detector should be selected to 177 wrap the reflective layer, but this study hopes to obtain better 178 position resolution. The figure3(c,d) shows the spectrum of 179 8-channel outputs in the horizontal direction (the same in the 180 vertical direction) with and without the reflective layer when 181 the center of the B-type detector is irradiated with a α source. 182 Due to the fixed irradiation position of the α source, theoret- 183 ically, the energy spectrum of each output should be in the

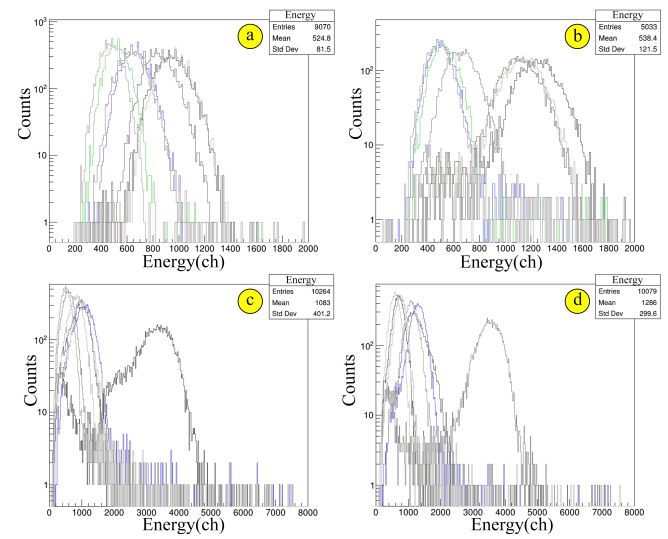


Fig. 3. the spectra of 8-channel SiPMs on the same side of the S-type detector when the interaction position is fixed at the center of the crystal: with the reflective layer(a), without the reflective layer(b); the spectra of 8-channel outputs of the B-type detector when the interaction position is fixed at the center of the crystal: with the reflective layer(c), without the reflective layer(d);

184 form of a Gaussian function. But in the case of wrapping the 185 reflective layer, the energy spectrum of each channel deviates 186 significantly from the Gaussian function. Because in this ex- 187 periment, trig is set "or". If the reflective layer is not wrapped, 188 it trig by fixed channel. But if wrapping the reflective layer, 189 many channels may trig, resulting in the energy spectrum not 190 the Gaussian function. Which may have a devastating impact 191 on the position reconstruction, so the B-type still adopts the 192 configuration without wrapping the reflective layer.

193 In order to improve energy resolution we will first measure 194 the total energy of the scattering and absorbing detectors, pick 195 out the events with the total energy as the full energy peak, 196 and use the total energy minus the energy of the scattering 197 detection to calculate the energy of the absorbing detector. In 198 the future, the energy resolution can be improved by optimiz- 199 ing the B-type detector adduction circuit, or directly changing 200 to the form of one by one readout.

C. The interaction position scale experiment

201 Interaction position scale experiments in the detector were 202 performed using the α source (Am-241, figure 4.b) and PCB 203 masks(figure 4.a). The thickness of the PCB mask is 2 mm, 204 and the hole diameter and the center spacing of adjacent holes 205 remain unchanged in the same PCB mask. Multiple PCB 206 masks with different hole diameters and hole spacing are used 207 in this experiment, such as a PCB with a hole diameter of 1 208 mm and a hole distance of 3.4 mm (PCB (ϕ 1.0, D3.4)). The 209 α source is placed in each hole in turn. The interaction po- 210 sition of these events is approximately considered to be the 211 same position, and its coordinates x,y are taken from the co-

213 ordinates of the center of the hole, and its coordinates z is a
 214 fixed value (1.5 mm for the S-type detector and 1.0 mm for
 215 the B-type detector).(figure 4.c)

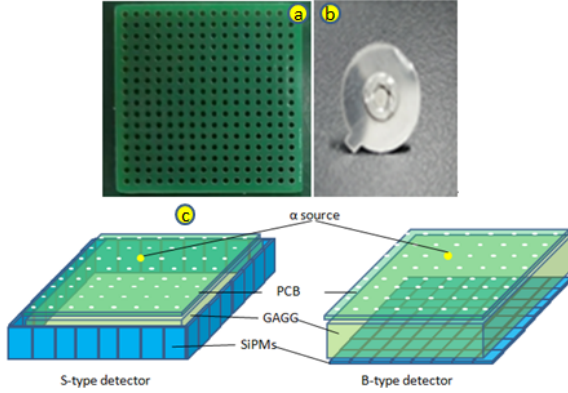


Fig. 4. The PCB mask(A), α source(B) The interaction position reconstruction experiment S-type and B-type detector(C)

216

218

III. ALGORITHM

219 In this study, two kinds of reconstruction algorithm is de-
 220 veloped to reconstruct the interaction position (x, y, z) where
 221 the γ -ray interacts with the detector: the response function
 222 method and the photon distribution reconstruction method. In
 223 both algorithm, z is taken as a fixed value. The response func-
 224 tion method can be used to reconstruct the interaction position
 225 only for S-type detector, it's not work for B-type detector. The
 226 photon distribution reconstruction method can be used in both
 227 types of detector.

228

A. The Response Function Method

229 Assuming that the scintillator is homogeneous and the flu-
 230 orescence photons are emitted uniformly in 4π , so more flu-
 231 orescent photons can be received, when the interaction point is
 232 closer to the SiPM. For example, the α sources are placed se-
 233 quentially at 8 test points in the black box in figure 5(left).
 234 E_{up} represents the energy deposited in the $SiPM_{up}$, and
 235 E_{down} indicates the energy deposited in the $SiPM_{down}$. As
 236 the position of the interaction changes, the E_{down}/E_{up} also
 237 changes, satisfying a certain response function, as shown in
 238 the figure 5(right). Repeating the above operations, the re-
 239 sponse functions of the whole detector (8 horizontal and 8
 240 vertical) can be obtained. Then the x,y values of any event
 241 can be reconstructed by using these response functions. This
 242 algorithm is only applicable in S-type detectors because simi-
 243 lar response functions cannot be obtained in B-type detectors.

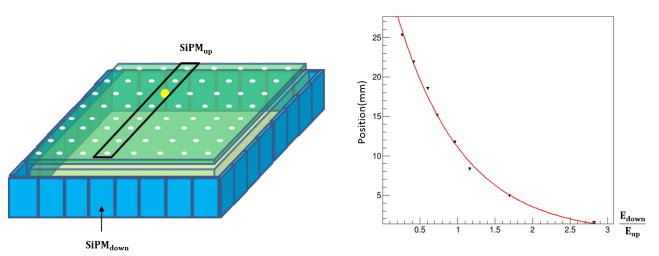


Fig. 5. 8 test points in a row(left), the response function(right)

244

B. The Photon Distribution Reconstruction Method

245 When a single fluorescent photon is received by the SiPM,
 246 a pulse of a certain amplitude is produced as the output. When
 247 multiple fluorescent photons are received, the output signal
 248 is the superposition of all the fluorescent photon producing
 249 signals:

250

$$V_i = V_{i0} \cdot N_i \quad (1)$$

251 V_i is the amplitude of the output signal of the $SiPM_i$, N_i
 252 is the number of fluorescent photons received by the $SiPM_i$,
 253 V_{i0} is the amplitude of the output signal when the $SiPM_i$
 254 receives single fluorescent photon. The number of fluorescent
 255 photons received by the $SiPM_i$ is strongly correlated with
 256 the solid angle of the $SiPM_i$ subtended to the interaction
 257 position:

258

$$N_i = N_0 \cdot E \cdot \Omega_i \quad (2)$$

259 N_0 is the number of fluorescent photons per solid angle at
 260 the unit energy deposited, and E is the energy deposited at
 261 that point. Assuming that the fluorescence emission at the in-
 262 teraction position is uniform at 4π , ignoring the fluorescence
 263 attenuation caused by the self-absorption of the crystal, then
 264 the N_0 is only a fixed value related to the luminescence yield
 265 of the crystal. Ω_i is the solid angle of the SiPM i subtended
 266 to the interaction position, as show in figure 6.

267 The ADC value of the SiPM i output signal is ADC_i :

268

$$ADC_i = a_i \cdot V_i + b_i \quad (3)$$

269

a_i and b_i are the scaling coefficients of the signal amplitude
 270 with the ADC address, which can be obtained experimentally
 271 and are fixed values.

272

$$ADC_i = a_i \cdot V_{i0} \cdot N_0 \cdot E \cdot \Omega_i + b_i$$

273

$$= K_i \cdot E \cdot \Omega_i + b_i \quad (4)$$

274

275 When the unit energy is deposited in the crystal, the ADC
 276 value which the SiPM i receives photons in the unit solid an-
 277 gle can be calculated using the formula (4). K_i, b_i are the
 278 conversion coefficient, can be measured experimentally. Be-
 279 fore introduce the experiment, let's explain how to calculate
 280 Ω_i .

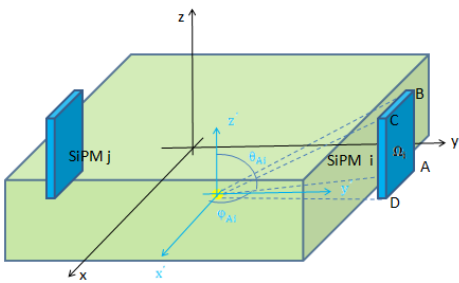


Fig. 6. The solid angle of the SiPM i and SiPM j subtended to the interaction position.

Taking the crystal center as the origin (0,0,0) of the xyz coordinate , the spatial coordinates of the 32 SiPMs have been determined, which is a known quantity. Taking *SiPM_i* as an example, the coordinates of point A (x_{Ai}, y_i, z_{Ai}), point B (x_{Bi}, y_i, z_{Bi}), point C coordinates (x_{Ci}, y_i, z_{Ci}), and point D coordinates (x_{Di}, y_i, z_{Di}). y_i is fixed values for the same SiPM . In this case, if an interaction occurs at any position in the crystal (x,y,z), the solid angle of *SiPM_i* relative to the interaction position can be Ω_i obtained by integrating φ_{Ai} and θ_{Ai} in the $x' y' z'$ coordinate system. In the $x' y' z'$ coordinate system, the coordinates of the relative interaction positions of ABCD points are transformed into A($x_{Ai}-x, y_i-y, z_{Ai}-z$), point B coordinates ($x_{Bi}-x, y_i-y, z_{Bi}-z$), point C coordinates ($x_{Ci}-x, y_i-y, z_{Ci}-z$), and point D coordinates ($x_{Di}-x, y_i-y, z_{Di}-z$). There will be a slight change in θ during the integration from point A to point D, but this change is negligible unless the interaction position is very close to the SiPM. So in the following integration process, θ is considered unchanged from point A to point D.

$$\Omega_i = \int_{\varphi_{Ai}}^{\varphi_{Di}} \int_{\theta_{Ai}}^{\theta_{Bi}} \sin\theta d\theta d\varphi \quad (5)$$

$$= \int_{\varphi_{Ai}}^{\varphi_{Di}} ((-\cos\theta_{Bi}) - (-\cos\theta_{Ai})) d\varphi \quad (6)$$

$$\cos\theta_{Ai} = \frac{z_{Ai} - z}{\sqrt{((y_i - y) \cdot \frac{1}{\tan\varphi_{Ai}})^2 + (y_i - y)^2 + (z_{Ai} - z)^2}} \quad (7)$$

suppose:

$$k_{Ai} = \frac{y_i - y}{z_{Ai} - z} \quad (8)$$

SO:

$$\cos\theta_{Ai} = \frac{1}{\sqrt{(\frac{k_{Ai}}{\sin\varphi_{Ai}})^2 + 1}} \quad (9)$$

in the same way:

$$\cos\theta_{Bi} = \frac{1}{\sqrt{(\frac{k_{Bi}}{\sin\varphi_{Bi}})^2 + 1}} \quad (10)$$

Substituting the formula(5), formula(6) into the formula(3):

$$\Omega_i = \int_{\varphi_{Ai}}^{\varphi_{Di}} \left(\frac{1}{\sqrt{(\frac{k_{Ai}}{\sin\varphi_{Ai}})^2 + 1}} - \frac{1}{\sqrt{(\frac{k_{Bi}}{\sin\varphi_{Bi}})^2 + 1}} \right) d\varphi \quad (11)$$

Here by looking up the indefinite integral table:

$$\int \frac{1}{(\frac{k}{\sin x})^2 + 1} dx = \quad (12)$$

$$\frac{\sqrt{-1 - 2k^2 + \cos^2 x} \cdot \csc x \cdot \log(\sqrt{2} \cdot \cos x + \sqrt{-1 - 2k^2 + \cos 2x})}{\sqrt{2 + 2k^2 \cdot \csc^2 x}} \quad (13)$$

$$k : \text{constant} \quad (14)$$

Equation (13) contains plural terms, but after merging and sorting, the plural terms are no longer existing, and the final result is:

$$\begin{aligned} \Omega_i = & \arctan\left(\frac{\sqrt{2k_{Ai}^2 + 2\sin^2\varphi_{Ai}}}{\sqrt{2}\cos\varphi_{Ai}}\right) - \arctan\left(\frac{\sqrt{2k_{Ai}^2 + 2\sin^2\varphi_{Di}}}{\sqrt{2}\cos\varphi_{Di}}\right) \\ & + \arctan\left(\frac{\sqrt{2k_{Bi}^2 + 2\sin^2\varphi_{Ai}}}{\sqrt{2}\cos\varphi_{Ai}}\right) - \arctan\left(\frac{\sqrt{2k_{Bi}^2 + 2\sin^2\varphi_{Di}}}{\sqrt{2}\cos\varphi_{Di}}\right) \end{aligned} \quad (15)$$

$$\sin\varphi_{Ai} = \frac{y_i - y}{\sqrt{(y_i - y)^2 + (x_i - x)^2}} \quad (16)$$

$$\cos\varphi_{Ai} = \frac{x_i - x}{\sqrt{(y_i - y)^2 + (x_i - x)^2}} \quad (17)$$

The transformations of φ_{Bi} and φ_{Di} are similar to those of φ_{Ai} .

The solid angle of the any interaction position to SiPMi can be calculated now. Next, the K_i, b_i are measured experimentally.A α source was placed at any position in the crystal, the solid angle of the 32-channel SiPMs were theoretically calculated, and the ADC value of the 32-channel SiPMs were recorded experimentally. Then, the position of the α source was changed, the solid angle of the 32-channel SiPMs were calculated theoretically, and the ADC value of the 32-channel SiPMs were recorded experimentally. Theoretically, the values of K_i, b_i can be obtained in two experiments, and in order to reduce the experimental error, the method of multiple experimental iterations of K_i, b_i is adopted. The decision condition for the iteration is that the difference between the center value of the 32-channel SiPMs experimental energy spectrum

(the blue line in figure 7) and the theoretical calculated expected value (the red line in figure 7) is the smallest. The figure 7 shows the comparison of the 32-channel experimental energy spectrum and the theoretical calculated expected value at a certain experimental point. The K_i, b_i ensure that the total difference between the theoretical and experimental values of the 32 SiPMs is smaller, so the experimental center value is slightly different from the theoretical calculated value in some SiPMs.

The Photon Distribution Reconstruction Method is not directly using the ADC value to calculate the position. The values of the 32-channel ADC at the interaction position can be calculated using Equation (4). First, 32-channel ADC values are counted as a set of data at one interaction position. Then change the interaction position to get another set of data. Finally, repeat the process to make a database. When an unknown interaction position event occurs, a set of 32-channel ADC values is obtained, and the 32 ADC values are compared with each set of data in the database to find the most similar set of interaction position. The set that can best reproduce the photon distribution of the signal is the reconstructed position. Therefore, the larger the database, the higher the accuracy of the reconstruction. Experimentally, it's hard to make a large database. But using Equation (4), we can make a database of any size.

The solid angle of the SiPMi relative to any interaction position in the figure 6 can be calculated using the formula (15), which is only a schematic diagram of the S-type detector. If the crystal in the figure 6 is compressed in the y direction and elongated in the z direction, the schematic diagram of the B-type detector is obtained, so the formula (15) is still valid for the B-type detector. Therefore, the photon distribution reconstruction method can also be applied to B-type detectors.

375

IV. RESULT

376 A. The reconstruction result of the Response function method

377 Figure 8 shows the experimental results of the reconstruction using PCB ($\phi 1.0$, D3.4) using the response function method. The red dot is the hole position of PCB ($\phi 1.0$, D3.4) in the experiment, and the black dot is the central value of the reconstruction position, and the uncertainty is the FWHM (full width at half maximum) of the reconstruction position of the same hole event. Approximately 3,000 reconstruction events were counted at each experimental site.

385 As can be seen from the figure, the central value of the reconstruction position is basically the same as the experimental position, the average deviation of the 64 experimental points is about 0.3 mm (both the x and y direction). There is obvious deviation in data of the second to last, around 5 mm in vertical axis, comparing with other results. The reason is that the response function in figure 5 (right) changes rapidly around 5 mm. Due to the lack of experimental points, the response function cannot well describe the trend change of this part, resulting in poor position reconstruction results in this part. The uncertainty of the reconstruction position is rela-

tively large. The main reason for these problems is that only part of the fluorescent photons are collected by each SiPM, and the statistical fluctuation of the fluorescence photon number is very large, so it is necessary to use as many SiPMs as possible to reduce the impact of statistical fluctuations when reconstructing the location.

402 B. The reconstruction result of the Photon Distribution 403 Reconstruction Method.

404 The reconstruction results of the photon distribution reproduction method are shown in figure 9 (S-type detector, PCB
405 ($\phi 1.0$, D3.4), left) and figure 9 (B-type detector, PCB ($\phi 1.0$,
406 D3.4), right). The red dot is the hole position of PCB ($\phi 1.0$,
407 D3.4) in the experiment, and the black dot is the central
408 value of the reconstruction position, and the uncertainty is
409 the FWHM (full width at half maximum) of the reconstruc-
410 tion position of the same hole event. Approximately 3,000
411 reconstruction events were counted at each experimental site.

412 The whole crystal is divided into two parts: the middle 6*6
413 36 experimental points and the outermost circle of 28 exper-
414 imental points, the middle 6*6 is called the central part, and
415 the outermost circle is called the edge part. For the S-type
416 detector, the average deviation of the experimental points is
417 about 0.3 mm (both the x and y direction) in the central part,
418 which is same as the response function method. For the B-
419 type detector, the average deviation of the experimental points
420 is about 0.4 mm (both the x and y direction) in the central part,
421 which is slightly higher than the response function method. In
422 the edge part, the average deviation become 0.5 mm (both the
423 x and y direction) for the S-type detector, and 0.7 mm for the
424 B-type detector. Because the closer to the edge of the crys-
425 tal, the more serious the damage to the position information
426 caused by the optical scattering of fluorescence.

427 The above reconstruction results show that the event with
428 the interaction location at the edge part of the detector is not
429 as good as the event in the center part. In the next experiment
430 to determine the position-resolved limit, the edge part of the
431 event will not be considered, and the event in the center of the
432 detector will be mainly focused.

434 C. The position-resolved limit experiments

435 The position resolution limit has been investigated by ap-
436 plying PCB masks with the different hole spacing. In order
437 to reduce the uncertainty of the interaction position caused
438 by the hole size, the hole diameter of the PCB board with a
439 hole spacing of less than 2 mm is changed to 0.5 mm. Figure
440 10(up) shows the position reconstruction result (x-direction
441 projection) using the PCB($\phi 0.5$, D1.2) for the S-type detector,
442 and Figure 10(down) shows the position reconstruction result
443 (x-direction projection) using the PCB($\phi 0.5$, D1.6) for the B-
444 type detector.

445 The reconstruction algorithm used in the position-resolved
446 limit experiment is the photon distribution reproduction
447 method, which is used for both S-type and B-type detectors.

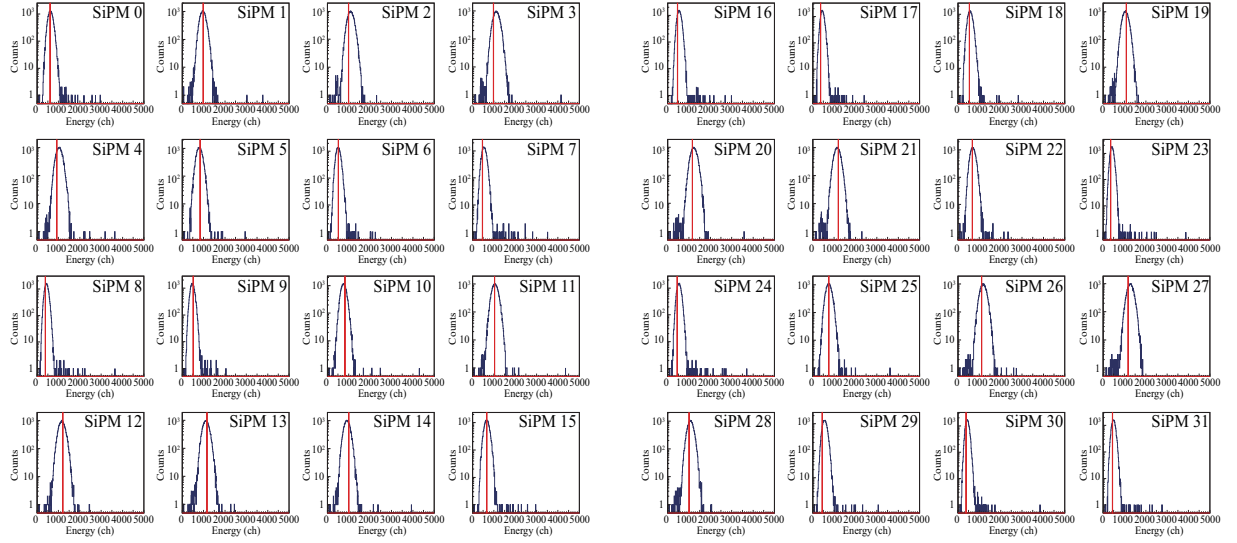


Fig. 7. the 32-channel experimental energy spectrum(blue line) and the theoretical calculated expected value(red line) at a certain experimental point

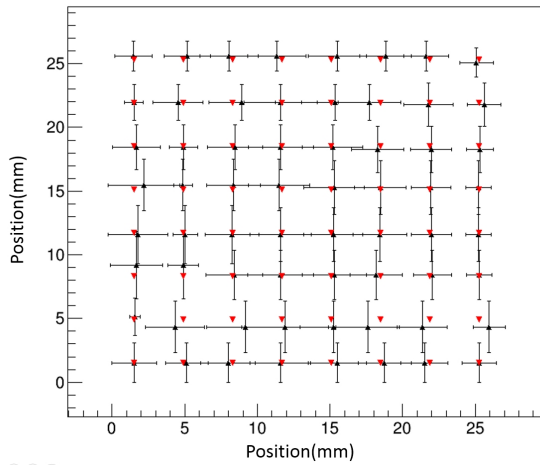


Fig. 8. The reconstruction result of the response function method(S-type detector, PCB (1.0, 3.4))

The figure 10(up) shows a total of 11 peaks from 8 mm to 22 mm, and the average spacing between the two peaks is about 1.27 mm, which is basically the same as the 1.2 mm hole spacing of the PCB board, indicating that the position resolution limit of the S-type detector is about 1.2 mm.

The figure 10(down) shows a total of 12 peaks from 5.5 mm to 26 mm, and the average spacing between the two peaks is about 1.71 mm, which is slightly larger than the 1.6 mm hole spacing on the PCB board, indicating that the position resolution limit of the B-type detector is about 1.6 mm. The reason why the position resolution limit is 1.6 mm instead of the more conservative 1.7 mm is that except for peaks 2,3 and 9,10, which overlap significantly, the other peaks are very well distinguished, which should further reduce the hole spacing of the PCB. The reason for the overlap of peaks 2,3

and peaks 9,10 is that the positions of the holes of peaks 3 and 9 are exactly the gap positions of the two SiPMs in the SiPM array, and the gap width of the two SiPMs is about 0.43 mm, which is basically the same as the hole diameter of the PCB board of 0.5 mm. When the interaction sites are located at peaks 3 and 9, a large number of fluorescent photons are not received by the SiPMs, but escape through the gap between the SiPMs, which also explains why the counts at peaks 3 and 9 are significantly smaller. This problem does not exist for the S-type detector, where the S-type detector uses 32 SiPMs for position reconstruction at the same time, and when the interaction position is in the gap between one of the two SiPMs, the remaining 30 SiPMs can be used for position reconstruction without particularly affecting the reconstruction results.

477 V. THE COMPTON CAMERA PRINCIPLE PROTOTYPE 478 AND PERFORMANCE TESTING

A double-layer Compton Camera based on monolithic crystals was built, with an S-type detector as the scattering detector and a B-type detector as the absorption detector(figure 1.e). The spacing between the scattering detector and the absorption detector was 20 mm. Cs-137 point source (about 1 mm in diameter) was used as the imaging object in this study. The Cs-137 was placed two positions 27 mm away from the vertical direction of the scattering detector, and the two positions were 8 mm apart in the same imaging plane. Both the S-type detector and the B-type detector use the Photon Distribution Reconstruction Method to reconstruct the interaction position. Figure 11 shows the reconstruction results for the two positions. Use the FWHM of the reconstruction result as the spatial resolution, so the spatial resolution at 27 mm is about 5.4 mm.

Compared with the existing Compton Cameras, Turecek et al.[28] developed a double-layer Compton Camera composed

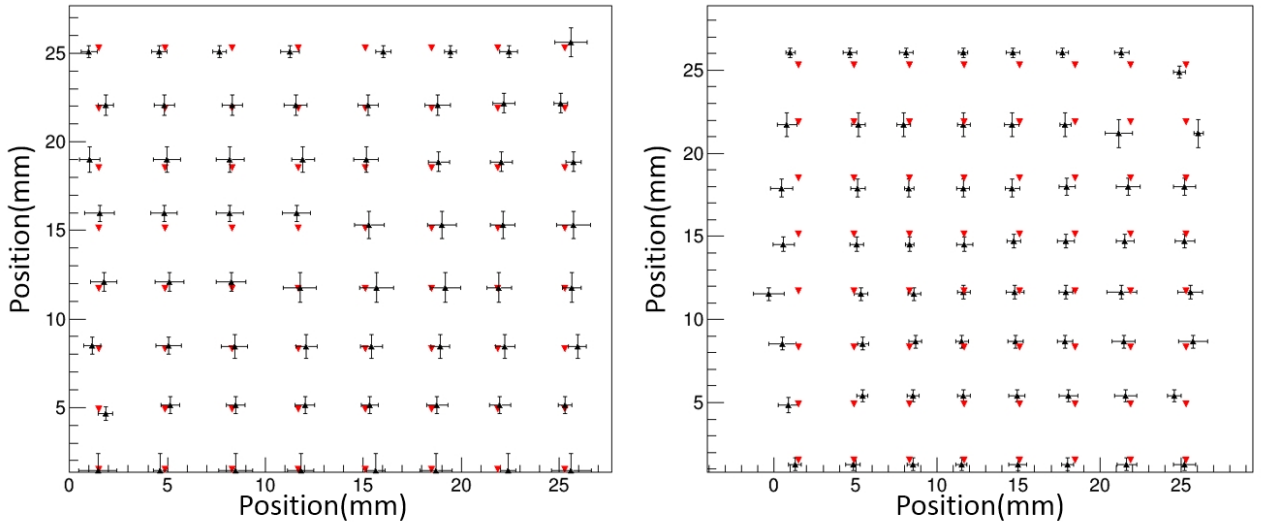


Fig. 9. The reconstruction result of the S-type detector(left) and B-type detector(right) using the photon distribution reconstruction method (PCB ($\phi 1.0$, D3.4))

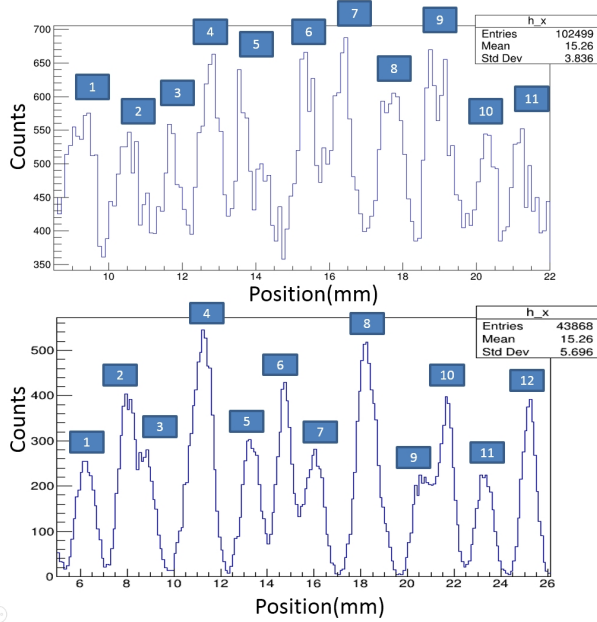


Fig. 10. The limit of position resolution of S-type detector-PCB(1.2,up).The limit of position resolution fo B-type detector-PCB(1.6,down)

504 detector is much lower than that of the semiconductor de-
505 tector. However, the high processing cost of semiconductor
506 detectors, harsh working conditions and complex electronic
507 systems make it difficult to commercialize semiconductor-
508 based Compton Cameras at low cost. The Compton Cam-
509 era based on the monolithic scintillator crystal built in this
510 study is low-cost, simple in structure, and slightly lower in
511 detection performance than the semiconductor-based Com-
512 ton Camera, which undoubtedly has greater possibilities in
513 low-cost commercialization.

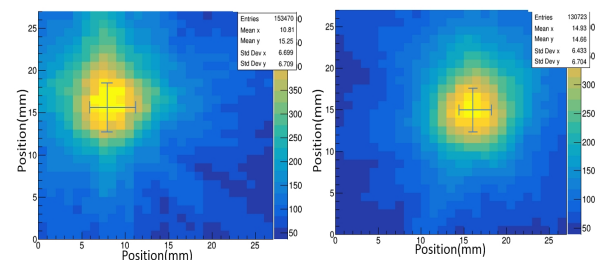


Fig. 11. The reconstruction results of Cs-137 at two points(8mm apart).

496 of a 1 mm thick silicon detector and a 2 mm thick CdTe detec-
497 tor based on the pixel array semiconductor detector Timepix3,
498 with a spatial resolution of up to 2.5 mm at 25 mm, which
499 is one of the Compton Cameras with the most ideal imag-
500 ing effect of the double-layer semiconductor detector struc-
501 ture today. The spatial resolution of the Compton Camera
502 based on the whole scintillator is lower than that of the detec-
503 tor, mainly because the energy resolution of the scintillator

516

VI. DISCUSSION

517 Most of the existing Compton Cameras use pixelated crys-
518 tals to determine the position of the interaction position.[29,
519 30] There is no doubt that the higher pixelation, the higher
520 accurate we can get. But as the level of pixelation increases,
521 a series of problems arise. The following discussion only
522 considers the case where the detector is scintillator detector,

523 and does not consider the case where the detector is semi-
 524 conductor detector or gas detector. 1. The processing dif-
 525 ficulty and cost of crystals will inevitably increase, and the
 526 level of pixelation cannot be increased indefinitely. Taking
 527 the 27*27*3 mm GAGG crystal used in this study as an ex-
 528 ample, if the pixelated crystal method is used to achieve 1.2
 529 mm position resolution, the crystal pixels need to be divided
 530 into a 1.2*1.2*3 mm 23*23 array, and the processing cost
 531 will become 3-4 times. 2. In order to determine the inter-
 532 action position, each pixel needs to have an independent data
 533 acquisition, with the increase of the level of pixelation, the ac-
 534 quisition system will become very redundant, and the redund-
 535 ant acquisition system will bring problems such as reduced
 536 signal-to-noise ratio and serious crosstalk. Taking this study
 537 as an example, a total of 32-channels of data acquisition are
 538 required for the S-type detector, and 529-channels(23*23) of
 539 data acquisition are required to achieve the same position res-
 540 olution if the traditional one crystal is used instead. Of course,
 541 some new schemes have been developed, in which a data ac-
 542 quisition can correspond to multiple pixelated crystals, and
 543 then the algorithm is used to reconstruct the interaction posi-
 544 tion, but the position resolution cannot be guaranteed, and the
 545 difficulty of the algorithm is increased.[31] 3. Because the
 546 pixelated crystal must be coupled with the acquisition system
 547 one by one, its configuration can only be similar to the B-type
 548 detector in this study, and if the multi-layer B-type detector is
 549 used, there must be γ -ray to react with the electronic device
 550 instead of the crystal, which reduces the detector efficiency.
 551 The use of multi-layer S-type detectors will greatly reduce the
 552 efficiency degradation caused by this phenomenon.

553 In this study, we proposed a method for reconstructing the
 554 interaction position in monolithic crystals, and achieved good
 555 reconstruction accuracy, which can be used in many fields.
 556 In the study of nuclear reactions and nuclear structure, track
 557 measurement is an important research method, usually using
 558 equipment such as solid track detectors, ionization chambers
 559 or time projection chambers[32, 33], which mainly respond
 560 to charged particles and have low detection efficiency for γ -
 561 rays. In the future, the technology in this study can be used
 562 to combine multiple S-type detectors into a telescope detector
 563 system, which will obtain a good γ -rays trace. In the field of
 564 medical imaging, both single-photon emission computed to-
 565 mography (SPECT) and positron emission tomography (PET)
 566 require accurate measurements of the interaction position of
 567 γ -rays. The detectors currently used are semiconductor de-
 568 tectors (CdTe, CZT, etc.) or pixelated scintillator detectors
 569 (CLYC, CsI,etc.)[34, 35]. The technology in this study can

570 reduce costs, simplify the system structure, and improve the
 571 detection accuracy. In addition, this technology has the op-
 572 portunity to play a role in the fields of μ imaging, radioactive
 573 survey, radiation protection, etc.

574 This study is only a preliminary study of the raction po-
 575 sition reconstruction and the construction of Compton Cam-
 576 eras using monolithic crystals, and there is still a lot of work
 577 to be done. First of all, the S-type detector used a thin slice
 578 structure in this study, and the thickness of 3 mm can only be
 579 coupled with a layer of SiPM, which makes the z-direction
 580 cannot be determined, and only a fixed value can be taken. In
 581 the future, the thickness of the crystal can be increased, mul-
 582 tilayer SiPM can be coupled, and the photon distribution can
 583 be used to determine the position in the z-direction. Secondly,
 584 the algorithm used in this study only considers the solid angle,
 585 but does not consider the optical transmission properties of
 586 photons in the crystal, which leads to the deterioration of the
 587 reconstruction accuracy of the edge part, and the optical trans-
 588 mission properties can be added to the algorithm to improve
 589 the reconstruction accuracy in the future. For the Compton
 590 Camera, the S-type detector is used as the scattering detec-
 591 tor and the B-type detector is the two-layer configuration of
 592 the absorption detector, and the configuration of the multi-
 593 layer S-type detector can be used to improve the detection
 594 efficiency in the future.

VII. CONCLUSION

595 In this paper, a prototype Compton Camera based on a
 596 monolithic GAGG crystal is built, with the S-type detector
 597 as the scattering detector and the B-type as the absorption de-
 598 tector. With two types of position reconstruction algorithm
 599 developed in the present work, the interaction position in
 600 the scattering and the absorption detectors can be determined
 601 with the resolution of 1.2 mm and 1.6 mm, respectively. Us-
 602 ing Cs-137 as a point source, the position of the source can be
 603 determined with a resolution of 5.4 mm when the source was
 604 27 mm away from the scattering detector.

605 The monolithic crystal based Compton Camera developed
 606 in the present work has the advantages of low cost, simple
 607 and compact in structure. The moderate imaging performance
 608 also meets the requirements of the radioactive source posi-
 609 tioning and nuclear medicine in nuclear industry applications.
 610 These facts show the high potential of the monolithic crystal
 611 based Compton Camera to be commercialized.

613 [1] R.W.Todd, J.M.Nightingale, D.B.Everett, A proposed camera. 621
 614 Nature (251), 132-134(1974). doi: 10.1038/251132A0.
 615 [2] Z. Yao, Y. Yuan, J. Wu et al., Rapid Compton camera imag- 622
 616 ing for source terms investigation in the nuclear decommission- 623
 617 ing with a subset-driven origin ensemble algorithm. Radiat. 624
 618 Phys. Chem. 197, 110133 (2022).doi:10. 1016/j. radph- 625
 619 yschem. 2022.110133
 620 [3] J. Zhang, X. Liang, J. Cai et al., Prototype of an array 626
 621 SiPM-based scintillator Compton camera for radioactive ma-
 622 terials detection. Radiat. Detect. Technol. 3(3), 17 (2019).
 623 doi:10.1007/s41605- 019- 0095-1
 624 [4] F. Tian, C. Geng, Z. Yao et al., Radiopharmaceutical imaging
 625 based on 3D-CZT Compton camera with 3D-printed mouse
 626 phantom. Phys. Medica 96, 140–148 (2022). doi:org/ 10.
 627 1016/j.ejmp. 2022. 03. 005
 628 [5] R. Wu, C. Geng, F. Tian et al., GPU-accelerated three-

dimensional reconstruction method of the Compton camera and its application in radionuclide imaging. Nucl. Sci. Tech. 34(4), 52 (2023). doi:org/ 10. 1007/ s41365- 023- 01199-y

[6] Z. Yao, Y. Xiao, B. Wang et al., Study of 3D fast compton camera image reconstruction method by algebraic spatial sampling. Nucl. Instrum. Meth. A 954, 161345 (2018). doi: org/ 10. 1016/j.nima. 2018. 10. 023

[7] Z. Yao, C. Shi, F. Tian et al., Technical note: rapid and highresolution deep learning-based radiopharmaceutical imaging with 3D-CZT Compton camera and sparse projection data. Med. Phys.49(11), 7336–7346 (2022). doi:org/ 10. 1002/ mp. 15898

[8] Inc H. D. H100 Gamma-Ray Imaging Spectrometer[EB/OL]. <https://h3dgamma.com/H100Specs.pdf>, 2022.2.3

[9] PHDS C. GeGI Gamma-Ray Imaging Spectrometer[EB/OL]. <https://phdsco.com/wp-content/uploads/2022/02/20220216-GeGI-Front-and-Back.pdf>,2022.2.3.

[10] Shinichiro T., Atsushi H., Yuto I.,et al. A Portable Si/CdTe Compton Camera and its Applications to the Visualization of Radioactive Substances. Nuclear Instruments and Methods in Physics Research Section A: Accelerators, Spectrometers, Detectors and Associated Equipment,doi:10.1016/J.NIMA.2014.11.119

[11] Xiaofeng G., Qingpei X., Dongfeng T.,et al. Simulation Study of the Backward-Scattering Effect in Compton Imager. Applied Radiation and Isotopes, 2017,124:93-99.doi:10.1016/j.apradiso.2017.03.019

[12] Liu Y., Fu J., Li Y.,et al. Preliminary Results of a Compton Camera Based On a Single 3D Position-Sensitive CZT Detector. Nuclear Science and Techniques,2018,29(10):145.doi:org/10.1007/s41365-018-0483-0

[13] Zhang Jipeng, Ma Xinhua, Zhang Bin et al.Simulation design and performance evaluation of the wide-energy range gamma-ray imaging detectors.Scientia Sinica(Technologica), 2024, 54: 31–42.doi: 10.1360/SST-2022-0411

[14] H. Muraishi, R.Enomoto, H.Katagiri et al.Visualization of low-level gamma radiation sources using a low-cost, high-sensitivity, omnidirectional compton camera. J. Vis. Exp.2020,155, e60463.doi: 10.3791/60463 .

[15] Z. Yao, Y. Xiao, M. Dong et al., Development of a two-layer dense-pixel LYSO Compton camera prototype for prompt gamma imaging. Phys. Med. Biol. 68, 045008 (2023). doi: org/ 10.1088/1361-6560/acb4d8

[16] T.Watanabe, R.Enomoto, H.Muraishi et al.Development of an omnidirectional gamma-ray imaging compton camera for low-radiation-level environmental monitoring. J. Appl. Phys.2018,57,026401.doi: 10.7567/JJAP.57.026401.

[17] H. Katagiri, W. Satoh, R. Enomoto et al.Development of an all-sky gamma-ray Compton camera based on scintillators for high-dose environments. J. Nucl. Sci.Technol.2018,55, 1172–1179.doi: 10.1080/00223131.2018.1485598.

[18] H. Muraishi, R.Enomoto, H.Katagiri et al.Visualization of low-level gamma radiation sources using a low-cost, high-sensitivity, omnidirectional compton camera. J. Vis. Exp.2020,155, e60463.doi: 10.3791/60463 .

[19] R.K.Parajuli, M.Sakai, R. Parajuliet et al. Development and Applications of Compton Camera—A Review.Sensors 2022,22,7374. doi: 10.3390/s22197374.

[20] P.Buzhan.Silicon photomultiplier and its possible applications Nucl. Instrum. Methods Phys. Res. **504** 48–52. doi:10.1016/S0168-9002(03)00749-6.

[21] Min Li,Zhi-Min Wang,Cai-Mei Liu et al., Performance of compact plastic scintillator strips with wavelength shifting fibers using a photomultiplier tube or silicon photomultiplier readout. Nucl. Sci. Tech.**2020** 34:31.doi:10.1007/s41365-023-01175-6.

[22] Yu-Ying Li,Chang-Yu Li Kun Hu et al. Design and development of multi-channel front end electronics based on dual-polarity charge-to-digital converter for SiPM detector applications. Nucl. Sci. Tech.(2023) 34:18.doi:10.1007/s41365-023-01168-5

[23] Wei Lu,Lei Wang, Yong Yuan et al. Monte Carlo simulation for performance evaluation of detector model with a monolithic LaBr₃(Ce) crystal and SiPM array for γ radiation imaging. Nucl. Sci. Tech.(2022) 33:107.doi:10.1007/s41365-022-01081-3

[24] C.Z. Uche, W.H. Round, M.J. Cree, Evaluation of two compton Camera models for scintimammography. Nucl. Instrum. Meth. A.662(1), 55–60 (2012). doi:org/ 10.1016/j. nima.2011.09.058

[25] T.Yanagida , K.Kamada , Y.Fujimoto et al.Comparative study of ceramic and single crystal Ce:GAGG scintillator. Optical Materials **35**2480–2485(2013) doi:10.1016/j.optmat.2013.07.002.

[26] Wei-Jie Zhang, Qin-Hua Wei , Xiao Shen et al.Preparation and properties of GAGG:Ce/glass composite scintillation material. Chin. Phys. B. Vol. 30, No. 7 (2021) 074205. doi:10.1088/1674-1056/abe3ea

[27] Ji-Peng Zhang,Xiu-zuo Liang,Jia-le Cai et al.Prototype of an array SiPM-based scintillator Compton camera for radioactive materials detection. Radiation Detection Technology and Methods (2019) 3:17. doi:10.1007/s41605-019-0095-1

[28] D.Turecek, J.Jakubek, E.Trojanova et al.Compton camera based on Timepix3 technology. Journal of Instrumentation **13** C11022,doi:10.1016/j.optmat.2013.07.002.

[29] S.Takeda, S.Ishikawa, S.Odaka et al. A new Si/CdTe semiconductor Compton camera developed for high-angular resolution. In Hard X-Ray and Gamma-Ray Detector Physics IX; SPIE: Bellingham,WA, USA, 2007; **6706** pp:187-197.doi:10.1117/12.733840.

[30] E. Muñoz, J. Barrio, A. Etxeberria et al. A Performance evaluation of MACACO:a multilayer Compton camera. Physics in Medicine & Biology **62** (2017) 7321–7341 . doi:10.1088/1361-6560/aa8070.

[31] Ming-Hao Dong, Zhi-Yang Yao, Yong-Shun Xiao, Development and preliminary results of a large-pixel two-layer LaBr₃ Compton camera prototype. Nuclear Science and Techniques **34** (2023) 34:121.doi:10.1007/s41365-023-01273-5.

[32] Duan Xiaojiao, LanXiaofei , TanZhixin et al. Calibration of CR-39 with monoenergetic protons. Nuclear Instruments and Methods in Physics Research A 609(2009)190–193. doi:10.1016/j.nima.2009.08.061.

[33] Chuan Huang, Zhiguo Xu, Zulong Zhao et al. Carbon ion radiography with a composite ionization chamber detector. Applied Radiation and Isotopes 203 (2024) 111072.doi:10.1016/j.apradiso.2023.111072.

[34] Hai-Yan Du, Cheng-Bo Du, Karl Giboni et al. Screener3D: a gaseous time projection chamber for ultra-low radioactive material screening. NUCL SCI TECH (2021) 32:142. doi:org/10.1007/s41365-021-00983-y

[35] A. Kishimoto, J. Kataoka, T. Nishiyama, et al. Performance and field tests of a handheld Compton camera using 3-D position-sensitive scintillators coupled to multi-pixel photon counter arrays.J. Instrum. **2014** ,9,P11025 doi:0.1088/1748-0221/9/11/P11025.